IEEE Access
Multidisciplinary | Rapid Review | Open Access Journal

Received November 4, 2019, accepted November 15, 2019, date of publication November 21, 2019,
date of current version December 16, 2019.

Digital Object Identifier 10.1109/ACCESS.2019.2954842

Optimal Design and Tracking Control of a Superelastic Flexure Hinge Based 3-PRR Compliant Parallel Manipulator

MIAO YANG[1,2], CHI ZHANG[1,3], GUILIN YANG[1,3], (Member, IEEE), AND WEI DONG[2], (Senior Member, IEEE)

[1]Ningbo Institute of Materials Technology and Engineering, Chinese Academy of Sciences, Ningbo 315201, China
[2]State Key Laboratory of Robotics and System, Harbin Institute of Technology, Harbin 150080, China
[3]Zhejiang Key Laboratory of Robotics and Intelligent Manufacturing Equipment Technology and Engineering, Ningbo 315201, China

Corresponding author: Wei Dong (dongwei@hit.edu.cn)

This work was supported in part by the NSFC-Zhejiang Joint Fund for the Integration and Information under Project U1609206, in part by the National Natural Science Foundation of China under Project 51905523, in part by the Postdoctoral Science Foundation of China under Project 2019M652152, and in part by the Innovation Team of Key Components and Key Technology for the New Generation Robot under Project 2016B10016.

ABSTRACT A major obstacle that restricts the application of notched flexure hinge based compliant mechanism is its limited motion range. This paper presents the optimal design and tracking control of a superelastic flexure hinge based 3-PRR compliant parallel manipulator (CPM) to achieve high precision planar motion within centimeter's translation range and up to 10 degrees' rotational range. Firstly, a novel asymmetric ellipse-parabola (AEP) notch shape is proposed, and the geometric parameters of the AEP superelastic flexure hinge are acquired via multi-objective optimization to obtain desirable transmission performance. Secondly, a nominal inverse kinematic model of the CPM is established, and the dimension parameters of the 3-PRR manipulator are synthesized to maximize the dexterity of the CPM over the regular workspace. Thereafter, a disturbance observer based inverse kinematic control scheme (DOB-IKM) is proposed to suppress the model mismatches and external disturbances of the 3-PRR CPM, where the unmodeled factors of the system are approximated through an online learning radical basis function neural network (RBFNN) and the external disturbances of the CPM is observed and compensated by a disturbance observer (DOB). Finally, a prototype of the 3-PRR CPM is manufactured, and experimental tests show the effectiveness of the proposed control scheme and the superiority of the 3-PRR CPM.

INDEX TERMS Compliant parallel manipulator, inverse kinematics, superelastic flexure hinge, tracking control.

I. INTRODUCTION

Flexure hinges always serve as passive rotational joints in CPMs to transmit motion and force continuously. A lot of adverse effects in conventional rigid parallel manipulators can be eliminated by employing this transmission method, such as, backlash, friction, wear, and lubrication [1], [2]. Thus CPMs are capable of implementing tasks where high precision and high resolution are required [3], [4]. The notched flexure hinge is the most frequently used flexure hinge for it's simply structure and high transmission precision. However, the motion ranges of conventional notched flexure hinge based CPMs are mainly within micron scales due to the stress concentration at the outer edge of the flexure hinges' thinnest section [5], which severely restricts the application of CPMs.

With the development of modern precision engineering, CPMs with centimeter motion range are highly demanded in biomedical sciences and optical engineering, such as, scanning probe microscopy, lithography, and cell micromanipulation [6], [7]. A promising way to enlarge the motion range of notched flexure hinge based CPMs is to improve the deformability of the material which used to fabricate the flexure hinges. Shape memory alloy (SMA) may be the best candidate because of the superelasticity, whose maximum recoverable strain is about 6% [8], while the maximum recoverable strain of most metal materials is only 0.2-0.8% [9].

The associate editor coordinating the review of this manuscript and approving it for publication was Hassen Ouakad.

In our previous research [10], [11], we have investigated the deformation characteristics of the superplastic flexure hinge (flexure hinge fabricated by SMA) and found that the rotation range of the superelastic flexure hinge is 6 times larger than the one made of steel.

Besides the material, the notch shape of a flexure hinge also has significant influence on its transmission performance. A variety of notch shapes have been proposed in literature, such as the right circular flexure hinge [12], the elliptic flexure hinge [13], the parabolic flexure hinge, and the hyperbolic flexure hinge [14]. However, those profiles of notch shapes defined only by few parameters, which restricts the selection of the optimal flexure hinge. In [15] Zelenika proposed a notch shape constructed by a series of spline curves, which is too complicated to find an optimal notch of the flexure hinge. Therefore, a novel AEP notch shape that can deal with the trade-off between the diversity and the complexity of the optimization is proposed in this paper, and the geometric parameters of the AEP superelastic flexure hinge is obtained through multi-objective optimization to minimize the performance deviation between the superelastic flexure hinge and the ideal rotation joint.

In recent years, many 2 degrees of freedom (DOF) planar translational CPMs with notched flexure hinge have been developed, because of the limited deformability of the conventional notched flexure hinges, these manipulators are hard to obtain centimeter scale motion range [16]. Furthermore, compared with the 2-DOF translational parallel manipulator, the 3-DOF planar platform add the rotation about z-axis, which can be applied to adjust the orientation of the sample. Therefore, the 3-DOF CPM is more capable to perform precision manipulation tasks. To realize 3-DOF planar motion, the manipulator usually can be constructed by three possible parallel-kinematic configurations, i.e., 3-PRR, 3-PPR, and 3-RRR [17], [18]. In this paper, the 3-PRR configuration is adopted to construct the 3-DOF planar CPM, since it is easier to achieve a large rotational motion range than the other two configurations. In the proposed 3-PRR CPM, the prismatic joint (P) is the active joint and serves as the motion input, the two passive rotational joints (R) are implemented by the AEP superelastic flexure hinges to achieve high precision motion. The dimension parameters of the 3-PRR CPM are determined by an optimization procedure to maximize the dexterity of the CPM over the regular workspace.

The control strategy of the CPM is also crucial to achieve high precision motion. A nominal inverse kinematic model of the CPM can be formulated according to the geometric relationships of the CPM. However, it cannot be used to control the CPM directly, since there are many unmodeled factors in the 3-PRR CPM are not considered in that model, such as the rotation error of the AEP superelastic flexures, the material nonlinearity, the manufacture uncertainties, and the assembling errors [19]. To deal with the model mismatches and external disturbances of CPMs, many close-loop control strategies are proposed, such as the PID controller, sliding mode controller, robust controller and the adaptive neural network controller [20]–[22]. Among these control methods, the neural network is famous for the ability to learn and approximate any arbitrary nonlinear function, which can be used to address the uncertainties of mechanical systems [23], [24]. Therefore, for the proposed 3-PRR CPM, a DOB-IKM control scheme is designed, where the unmodeled kinematics of the CPM are estimated by an on-line learning RBFNN and the system disturbances are suppressed by a disturbance observer based feedforward compensation design.

The remainder of this paper is organized as follows: a novel AEP notch shape for the superelastic flexure hinge is presented in Section II, and multi-objective optimization is conducted on the notch parameters to obtain optimal comprehensive performance of the superelastic flexure hinge. Then, a nominal inverse kinematic model of the CPM is established, and the dimension parameters of the manipulator are optimized in Section III by applying that model. Afterwards, the DOB-IKM control scheme is proposed in Section IV to suppress the model mismatches and external disturbances of the 3-PRR CPM. In Section V, a prototype of the superelastic flexure hinges based 3-PRR CPM is fabricated using the optimized AEP superelastic flexure hinge and the optimized dimension parameters of the manipulator, and experiment tests are carried out to verify the performance of the control scheme. Finally, the conclusion of this paper is provided in section VI.

II. OPTIMIZATION OF THE SUPERELASTIC FLEXURE HINGE

A. THE AEP SUPERELASTIC FLEXURE HINGE

In order to obtain optimal comprehensive performance of a superelastic flexure hinge, the notch shape of the flexure hinge should be carefully chosen. Typically, the elliptic notched flexure hinge has larger motion range and lower rotation stiffness than the parabolic flexure hinge, while the parabolic flexure hinge has better motion accuracy than the elliptic flexure hinge [14]. Furthermore, as reported in [25], asymmetric notched flexure hinge has better transmission performance than symmetric one. Therefore, an AEP notch shape is proposed in this paper, and the schematic diagram of the proposed AEP notched flexure hinge is presented in Fig.1, where the profile of the AEP notch comprises two ellipse-parabola (EP) curves, namely, EP curve 1 and EP curve 2, and the two EP curves intersect at point p_3 which is also the minimum thickness point of the flexure hinge.

Each EP curve in Fig.1 is a combination of two smoothly connected elementary curves, i.e., an elliptic curve and a parabola. Taking EP curve 1 for example, curve s_2 is the elliptic arc, s_1 is the parabola, and point p_2 is the connection point. A coordinate frame oxy is assigned at the center of the flexure hinge's thinnest section, and the x axis of the coordinate system follows the length direction of the notch. Moreover, l denotes the length of the notch, λ denotes the length coefficient, h denotes the height of the notch, and t denotes the minimum thickness of the notch.

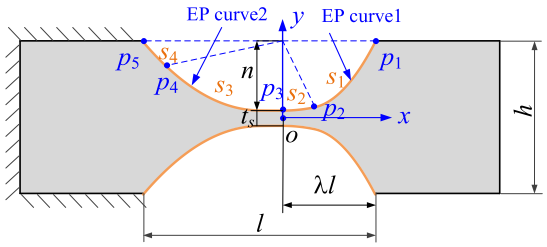

FIGURE 1. Schematic diagram of the AEP superelastic flexure hinge.

The center of the ellipse curve s_2 is located at $(0, h/2)$, and the parametric equation for the elliptic curve s_2 is given by

$$\begin{cases} x_{e1}(\varphi_1) = ne_1 \cos\varphi_1 & \varphi_{t1} \le \varphi_1 \le 0 \\ y_{e1}(\varphi_1) = n \sin\varphi_1 + h/2 & -\pi/2 \le \varphi_{t1} \le 0 \end{cases} \tag{1}$$

where $n = (h - t_s)/2$ denotes the length of the ellipse's vertical semi-axe, e_1 denotes the ellipticity of curve s_2, ne_1 denotes the length of the ellipse's horizontal semi-axe, φ_1 denotes the eccentric angle of s_2, and φ_{t1} denotes the terminated eccentric angle at the end point p_2.

The parabola curve s_1 is defined by two end points $p_1 = (\lambda l, h/2)$ and $p_2 = (ne_1 \cos\varphi_{t1}, n \sin\varphi_{t1} + h/2)$. Since the parabola curve s_1 and the ellipse curve s_2 are smoothly connected, they have the same slope at point p_2, i.e., $y'_{p1}(x = ne_1 cos\varphi_{t1}) = y'_{e1}(x = ne_1 cos\varphi_{t1})$. The curve function can be expressed as below

$$y_{p1}(x) = a_1 (x - ne_1 \cos\varphi_{t1})^2 + b_1 (x - ne_1 \cos\varphi_{t1}) + c_1 \tag{2}$$

where x satisfying $ne_1 \cos\varphi_{t1} < x < \lambda l$, and the coefficients are given as

$$\begin{cases} a_1 = (\lambda l \cos\varphi_{t1} - ne_1)/\left(e_1 \sin\varphi_{t1} (\lambda l - ne_1 \cos\varphi_{t1})^2\right) \\ b_1 = -1/(e_1 \tan\varphi_{t1}) \\ c_1 = h/2 + n \sin\varphi_{t1} \end{cases} \tag{3}$$

According to the geometric description, two constraints should be introduced to formulate EP curve 1. Firstly, the x coordinate value at point p_2 must be less than that at point p_1, i.e.,

$$g_{e1}(x) = ne_1 \cos\varphi_{t1} - \lambda l \le 0 \tag{4}$$

Secondly, the slope of the curve s_1 at p_1 must be positive, since the EP curve 1 is monotonic increasing, i.e.,

$$g_{p1}(x) = \lambda l \cos\varphi_{t1} - ne_1 \le 0 \tag{5}$$

Similarly, the equation for EP curve 2 can be obtained by changing the geometric parameters $(\lambda l, e_1, \theta_1)$ to $((1-\lambda)l, e_2, \theta_2)$ in Eq.(1) and Eq.(2), thus the elliptic curve s_3 is given by

$$\begin{cases} x_{e2}(\varphi_2) = ne_2 \cos\varphi_2 & \varphi_{t2} \le \varphi_2 \le -\pi/2 \\ y_{e2}(\varphi_2) = n \sin\varphi_2 + h/2 & -\pi \le \varphi_{t2} \le \pi/2 \end{cases} \tag{6}$$

and the parabola curve function is given as below

$$y_{p2}(x) = a_2 (x - ne_2 \cos\varphi_{t2})^2 + b_2 (x - ne_2 \cos\varphi_{t2}) + c_2 \tag{7}$$

where x satisfying $-(1-\lambda)l < x < ne_2 \cos\varphi_{t2}$, and the coefficients are given as

$$\begin{cases} a_2 = \dfrac{-(1-\lambda)l \cos\varphi_{t2} - ne_2}{e_2 \sin\varphi_{t2} ((1-\lambda)l + ne_2 \cos\varphi_{t2})^2} \\ b_2 = -1/(e_2 \tan\varphi_{t2}) \\ c_2 = (h/2 + n \sin\varphi_{t2}) \end{cases} \tag{8}$$

B. MULTI-OBJECTIVE OPTIMIZATION OF THE FLEXURE HINGE

A static deformation model that formulates the relationship between the end displacement and the external loads of an AEP superelastic flexure hinge can be established by using the modelling approach proposed in our previous work [11], which can be expressed by the following general function

$$(x_t, y_t, \theta_t) = \Gamma(\mathbf{g}, \mathbf{F}_e) \tag{9}$$

where x_t, y_t and θ_t are the displacements of the end point of the flexure hinge, $\mathbf{g} = (h, l, t_s, \lambda, e_1, \theta_1, e_2, \theta_2)$ is the geometric parameters of the flexure hinge, and $\mathbf{F}_e$ is the general planar end force.

In order to evaluate the transmission characteristics of the superelastic flexure hinge, the following four performance indices are introduced, i.e, the rotation range θ_{max}, rotation stiffness k_m, rotation error r_m, and the variation of center shift Δr [26]. θ_{max} represents the rotation angle of the superelastic flexure hinge when the maximum strain occurs at the outer edge of the flexure hinge up to the allowable strain (for safety, the allowable strain is set as 3% here), k_m represents the difficulty of a flexure hinge to deform under end moment, r_m represents the motion accuracy of a flexure hinge, Δr represents the stability of a flexure hinge under an external axial force. All the performance indices can be obtained based on the deformation model established in [11].

1) OPTIMIZATION GOAL

The flexure hinge is a substitution of the conventional rigid rotational joint in compliant mechanisms. Therefore, the optimization goal for the AEP superelastic flexure hinge is to minimize the deviation between the flexure hinge and the ideal rotational joint, which can be given as,

$$\begin{cases} k_m \to \min \\ r_m \to \min \\ \Delta r \to \min \end{cases} \tag{10}$$

2) DESIGN VARIABLES

Among the parameters which define the geometry of an AEP notched superelastic flexure hinge, h and l are determined by the size of the SMA stripe which used to fabricate the flexure hinge, and t_s is determined by the processing method. In this paper, we set $h = 10$mm, $l = 15$mm, and $t_s = 0.4$mm,

TABLE 1. Material properties of Nitinol alloy.

Property	Unit	Value
Modulus	[GPa]	Da=62.8, D_m=28
Transformation stresses	[MPa]	σ_s^{cr} =100 σ_f^{cr} =180
Stress-temperature slopes	[MPa/°C]	C_a = 12.8, C_m = 8
Transformation temperature	[°C]	As = 3.8, A_f = 14.5 M_s = -9.6, M_f = -12 T = 20
Transformation strain	[--]	ε_l = 3.2%

TABLE 2. Performance indices of the superelastic flexure hinges.

Performance index	The ellipse flexure hinge	The AEP flexure hinge	Improvement
rotation range θ_{max} (deg)	14.32	15.21	6.22%
rotation stiffness k_m *(Nmm/deg)*	5.27	4.76	-9.68%
rotation error r_m *(μm)*	19.7	14.1	-28.40%
variation of center shift Δr *(μm)*	1.10	1.07	-2.72%

and the remaining five parameters are selected as the design variables $\mathbf{X}$ to optimize the AEP notched superelastic flexure hinge,

$$\mathbf{X} = \{\lambda, e_1, \theta_1, e_2, \theta_2\} \tag{11}$$

3) OPTIMIZATION CONSTRAINTS

To guarantee that the established CPM has enough workspace, in this paper, the rotation range of the superelastic flexure hinge is designed to be larger than 15°. Considering the definition of the AEP notch, the optimization constraints are formulated as,

$$\begin{cases} \theta_{\max} > 15^{\circ} \\ g_{e1}(x) = ne_1 \cos\varphi_{t1} - \lambda l \le 0 \\ g_{p1}(x) = \lambda l \cos\varphi_{t1} - ne_1 \le 0 \\ g_{e2}(x) = ne_2 \cos\varphi_{t2} - (1-\lambda) l \le 0 \\ g_{p2}(x) = (1-\lambda) l \cos\varphi_{t2} - ne_2 \le 0 \end{cases} \tag{12}$$

where the subscripts 1 and 2 refer to EP curve 1 and EP curve 2, respectively.

4) BOUNDARY CONSTRAINTS

The boundary constraints of the optimization process are defined below,

$$\begin{cases} \lambda \in [0.2, 0.5] \\ e_1 \in [1, 4] \\ \varphi_{t1} \in [-\pi/2, 0] \\ e_2 \in [1, 4] \\ \varphi_{t2} \in [-\pi, -\pi/2] \end{cases} \tag{13}$$

5) OPTIMIZATION RESULTS

The NSGA-II algorithm is employed to find the solution of the multi-objective optimization problem formulated by Eq.(10)-(13), the initial population size is set as 200, and the number of generations is 50. The material which used to fabricate the AEP superelastic flexure hinge is Nitinol, which is the most frequently used SMA material. The constitutive parameters of Nitinol are measured by tensile tests and listed in Table 1, and detailed description of the material's constitutive parameters can be found in [11].

The geometric parameters of the selected AEP superelastic flexure hinge are $\lambda = 0.31$, $e_1 = 1.548$, $\varphi_{t1} = -1.524$, $e_2 = 3.12$, $\varphi_{t2} = -3.084$, and the performance indices of the flexure hinge are listed in Table 2. For comparison, the performance indices of an elliptic superelastic flexure hinge with the same notch length and minimum thickness of the optimized flexure hinge are presented in Table 1, which can be regarded as a special case of the AEP flexure hinge, i.e., $\lambda = 0.5$, $e_1 = 1.563$, $\varphi_{t1} = -\pi/2$, $e_2 = 1.563$, and $\varphi_{t2} = -\pi$.

It can be seen that the rotation range of the optimized superelastic flexure hinge is 15.21°, which is 6.22% higher than the elliptic flexure hinge. Meanwhile, the rotational stiffness, the rotation error and variation of the center shift are decreased by 9.68%, 28.4% and 2.72% respectively. The results above prove the superiority of the proposed notch shape and the effectiveness of the optimization process.

It also should be pointed out that if the AEP flexure hinge is fabricated by steel (the yield strain is 0.2%), the rotation range is only 2.43°, which is much smaller than the superelastic flexure hinge.

C. PERFORMANCE VERIFICATION

The performance indices of the optimized AEP superelastic flexure hinge have also been computed by the nonlinear finite element analysis (FEA) software ABAQUS to verify the effectiveness of the superelastic flexure hinge's deformation model. The FEA model of the optimized superelastic flexure hinge is shown in Fig.2, where the flexure hinge is scattered by C3D20 elements.

The simulated performance indices are as follows: the rotation range of the superelastic flexure hinge is $\theta_{max} = 15.52°$, the rotation stiffness is $k_m = 4.63$ Nmm/deg, the rotation error is $r_m = 14.45\mu$m, and the variation of center shift is $\Delta r = 1.16\mu$m. It can be seen that the performance indices obtained by the FEA simulation match well with those presented in Table 1 with a maximum relative error of 8.41%, which indicates the accuracy of the superelastic flexure hinge's deformation model.

III. DIMENSION OPTIMIZATION OF THE 3-PRR MANIPULATOR

A. STRUCTURE OF THE 3-PRR MANIPULATOR

The geometric schematic of a rigid 3-PRR parallel manipulator is presented in Fig.3. The fixed platform is an equilateral

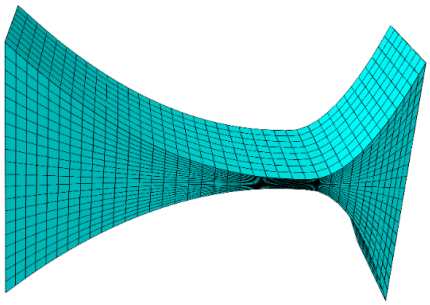

FIGURE 2. The FEA model of the optimized superelastic flexure hinge.

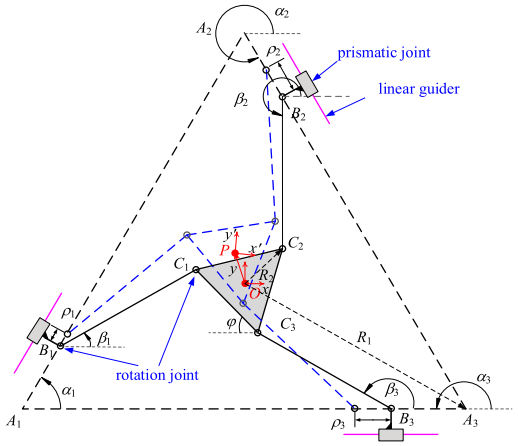

FIGURE 3. The 3-PRR planar parallel manipulator.

triangle defined by points A_1 to A_3, and the moving platform is also an equilateral triangle defined by points C_1 to C_3. Initially, the geometric center of the two platforms coincide at point O with a decline angle φ. Two Cartesian coordinate frames, the base frame Oxy and the moving frame Pxy, are assigned at the geometric center of the fixed base and the moving platform, respectively. The moving platform and the base platform are connected by three identical limbs, and each limb is actuated by a prismatic joint (P) and followed by two passive rotational joints (R). The circumradius of the base platform is denoted as R_1, and that of the moving platform as R_2, the length of the passive rigid link is denoted as L_l, and the orientation angles of the prismatic actuators $\alpha_i (i = 1, 2, 3)$ are 60°, −60° and 180°, respectively.

By replacing the passive rigid rotational joints in the rigid 3-PRR parallel manipulator with the optimized AEP superelastic flexure hinges, a 3-PRR CPM is established, as shown in Fig.4, where the rotation centers of the AEP superelastic flexure hinges coincide with their rigid counterparts, and the axial direction of the flexure hinges follows the length direction of the initial rigid links. Note that the two superelastic flexure hinges in one link are assembled in an alternate manner, so that the structure is symmetrical along the length direction of the link.

B. INVERSE KINEMATIC MODELING OF THE 3-PRR CPM

The inverse kinematic model of the 3-PRR CPM is used to establish the relationship between the given position and

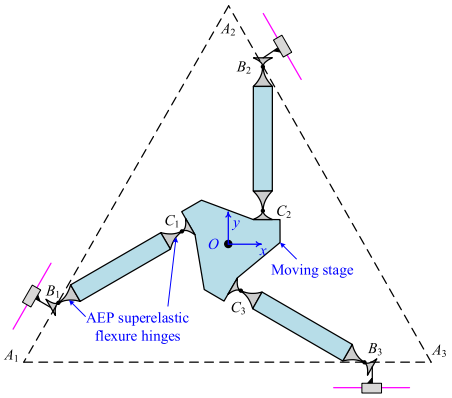

FIGURE 4. The superelastic flexure hinge based3-PRR CPM.

posture of the moving platform $\mathbf{y} = (x_P, y_P, \varphi_p)$ and the corresponding displacement of the three prismatic joints $\rho_i (i = 1, 2, 3)$. Since the rotation error of the AEP superelastic flexure hinge is much smaller than other flexure joints under the same rotation range (e.g., the flexure pivots) [27], a simple nominal inverse kinematic model of the 3-PRR CPM can be formulated without considering the rotation error of the superelastic flexure hinges. The vector constraint equation for the kinematic limb of the CPM can be given as below,

$$\mathbf{OP} + \mathbf{PC}_i = \mathbf{OA}_i + \mathbf{A}_i\mathbf{B}_i + \mathbf{B}_i\mathbf{C}_i \tag{14}$$

Rewritten Eq.(14) in the Cartesian space algebraically,

$$\begin{pmatrix} x_p \\ y_p \end{pmatrix} + R(\varphi_p + \varphi)\begin{pmatrix} x'_{Ci} \\ y'_{Ci} \end{pmatrix} = \begin{pmatrix} x_{Ai} \\ y_{Ai} \end{pmatrix} + (\rho_{i0} + \rho_i)\begin{pmatrix} \cos\alpha_i \\ \sin\alpha_i \end{pmatrix} + L_l\begin{pmatrix} \cos\beta_i \\ \sin\beta_i \end{pmatrix} \tag{15}$$

where, x'_{Ci} and y'_{Ci} are the coordinates of point C_i in the LCS, x_{Ai} and y_{Ai} are the coordinates of point A_i in the GCS, ρ_{i0} is the initial distance between point A_i and B_i, β_i is the angle of the links B_iC_i with respect to the x-axis of GCS, and the transformation matrix $\mathbf{R}(\bullet)$ is defined as $\mathbf{R}(\bullet) = \begin{pmatrix} \cos(\bullet) & -\sin(\bullet) \\ \sin(\bullet) & \cos(\bullet) \end{pmatrix}$.

According to Eq.(15), the displacement of the prismatic joint ρ_i can be solved as

$$\begin{cases} \rho_{i1} = \dfrac{-\chi_{i1} + \sqrt{\chi_{i1}^2 - 4\chi_{i2}}}{2} \\ \rho_{i2} = \dfrac{-\chi_{i1} - \sqrt{\chi_{i1}^2 - 4\chi_{i2}}}{2}, \end{cases} \tag{16}$$

where the coefficients in Eq.(16) are given as

$$\begin{cases} \chi_{i1} = 2\cos\alpha_i\chi_{i3} + 2\sin\alpha_i\chi_{i4} \\ \chi_{i2} = \chi_{i3}^2 + \chi_{i4}^2 - L_l^2 \\ \chi_{i3} = x_p + x'_{Ci}\cos(\varphi_P + \varphi) - y'_{Ci}\sin(\varphi_P + \varphi) - x_{Ai} \\ \qquad -\rho_{i0}\cos\alpha_i \\ \chi_{i4} = y_p + x'_{Ci}\sin(\varphi_P + \varphi) + y'_{Ci}\cos(\varphi_P + \varphi) - y_{Ai} \\ \qquad -\rho_{i0}\sin\alpha_i \end{cases} \tag{17}$$

Both ρ_{i1} and ρ_{i2} are feasible solutions of Eq.(15), however, considering the initial configuration of the manipulator as shown in Fig.4, ρ_{i1} is selected as the final solution of inverse kinematic problem.

Differentiating both sides of Eq.(15) with respect to time, yields

$$\dot{\boldsymbol{\rho}} = \mathbf{J}\dot{\mathbf{y}} \tag{18}$$

where $\dot{\boldsymbol{\rho}} = (\dot{\rho}_1, \dot{\rho}_2, \dot{\rho}_3)$ is the velocity vector of the prismatic joints, $\dot{\mathbf{y}} = \left(\dot{x}_p, \dot{y}_p, \dot{\varphi}_p\right)$ is the velocity vector of the moving platform, and $\mathbf{J}$ is the Jacobian matrix of the manipulator which can be expressed as

$$\mathbf{J} = \frac{1}{\mathbf{a}_i \cdot \mathbf{b}_i} \begin{pmatrix} \mathbf{b}_1 & (\mathbf{e}_1 \times \mathbf{b}_1) \cdot \mathbf{k} \\ \mathbf{b}_2 & (\mathbf{e}_2 \times \mathbf{b}_2) \cdot \mathbf{k} \\ \mathbf{b}_3 & (\mathbf{e}_3 \times \mathbf{b}_3) \cdot \mathbf{k} \end{pmatrix} \tag{19}$$

where $\mathbf{a}_i$ represents the unit vector of A_iB_i, $\mathbf{b}_i$ and $\mathbf{e}_i$ represent B_iC_i and P_iC_i respectively, $\mathbf{k}$ is a unit vector in z axis. They can be given as

$$\begin{cases} \mathbf{a}_i = (\cos\alpha_i, \sin\alpha_i, 0) \\ \mathbf{b}_i = L_l\,(\cos\beta_i, \sin\beta_i, 0) \\ \mathbf{e}_i = \begin{pmatrix} x'_{Ci}\cos(\varphi_P + \varphi) - y'_{Ci}\sin(\varphi_P + \varphi), \\ x'_{Ci}\sin(\varphi_P + \varphi) + y'_{Ci}\cos(\varphi_P + \varphi), 0 \end{pmatrix} \\ \mathbf{k} = (0, 0, 1) \end{cases} \tag{20}$$

The Jacobian matrix $\mathbf{J}$ represents the transformation between the parameter space and the operational space of the manipulator [28]. Because the 3-PRR manipulator has two translational DOFs and one rotational DOF, the last column in the Jacobian matrix has different units with the rest. A modified homogeneous Jacobian matrix is defined as [29]

$$\mathbf{J}_m = \mathbf{J}\,\mathrm{diag}\left(1, 1, \frac{1}{R_2}\right) \tag{21}$$

where R_2 is selected as the characteristic length.

C. DIMENSION OPTIMIZATION

As the geometric parameters of the 3-PRR manipulator have significant influence on its performance, optimization on the dimension parameters of the 3-PRR manipulator is implemented.

1) OPTIMIZATION GOAL

The reachable workspace of the 3-PRR manipulator can be obtained by utilizing the inverse kinematic model, but it is difficult to define and measure. Therefore, a cylinder in the reachable workspace is adopted to describe the regular workspace of the CPM, as shown in Fig.5. R_W is the radium of the cylinder and $2\varphi_{max}$ is the height of the cylinder. The manipulator can reach any point $(x_P, y_P\varphi_p)$ inside the cylinder.

The global conditioning index (GCI) is utilized as the kinematic index to evaluate the dexterity of the manipulator

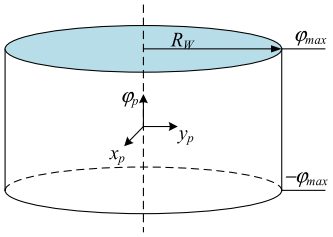

FIGURE 5. Schematic of the regular workspace.

over the workspace, which is given as [30]

$$C_W = \frac{\int_W \frac{1}{k} dW}{W} \tag{22}$$

where $k = \mathrm{cond}(\mathbf{J}_m)$ is the condition number of the homogeneous Jacobian matrix, W is the considered workspace of the manipulator, and C_w is a positive number less than 1 (the closer the value is to 1, the better dexterity of the manipulator).

The optimization goal is to maximize the GCI over the regular workspace, which can be expressed as

$$f = C_W \rightarrow \max \tag{23}$$

2) DESIGN VARIABLES

Based on the description of the manipulator, the optimization variable $\mathbf{X}$ is given as

$$\mathbf{X} = \{R_1, L_l, R_2, \varphi\} \tag{24}$$

3) OPTIMIZATION CONSTRAINTS

Since the rotation angles of the passive rotation joints should be within the motion range of the optimized AEP superelastic flexure hinges. The following constraints are introduced,

$$\begin{cases} \Delta\beta_i \le 15^\circ \\ \Delta\gamma_i \le 15^\circ \end{cases} \tag{25}$$

where $\Delta\beta_i$ and $\Delta\gamma_i$ are the rotation angles of the superelastic flexure hinges at point B_i and point C_i respectively.

In addition, as we want to design a 3-PRR CPM with a centimeter-scale translation range and a 10-degree rotation range, the following constrains are imposed in the optimization

$$\begin{cases} R_W \ge 10 \\ \varphi_{\max} \ge 5^\circ. \end{cases} \tag{26}$$

4) BOUNDARY CONSTRAINTS

The limitations for the dimension parameters of the manipulator and the rotation range of the superelastic flexure are given as

$$\begin{cases} R_1 \in [50, 150] \\ L_l \in [50, 150] \\ R_2 \in [25, 100] \\ \varphi \in \left[-\frac{\pi}{3}, \frac{\pi}{3}\right], \end{cases} \tag{27}$$

5) OPTIMIZATION RESULTS

By applying genetic algorithm, the geometric parameters of the CPM is finally calculated as $R_1 = 124.3$mm $R_2 = 25$mm $L_l = 75.77$mm and $\varphi = -46.07°$, the radius of regular workspace is $R_w = 10.198$ mm, and the GCI over the regular workspace of the manipulator is $C_w = 0.88$. The value of GCI is very close to 1, which indicates the manipulator has good kinematic performance in the regular workspace.

IV. CLOSE-LOOP CONTROL SCHEME DESIGN

The inverse kinematic model established above provides a simple and analytic solution for the 3-PRR CPM. Unfortunately, it cannot be directly used to control the manipulator, because it does not consider some factors of the system, such as the parasitic motion of the flexure hinges, the hysteresis mechanical behavior of the SMA, the manufacturing uncertainties, the assembling error of the CPM, and external disturbances, which may deteriorate the motion accuracy of the manipulator.

The complete inverse kinematic model of the 3-PRR CPM can be given in the following discrete form

$$\boldsymbol{\rho}(k) = \boldsymbol{\rho}_n(k) + \boldsymbol{\rho}_a(k) + \mathbf{d}(k) \tag{28}$$

where $\boldsymbol{\rho}_n$ represents the nominal inverse kinematic model of the CPM which is established in section III, $\boldsymbol{\rho}_a$ represents the unmodeled kinematics of the CPM, and $\boldsymbol{d}(k)$ represents the external disturbances. Accordingly, in this section we proposed a DOB-IKM control scheme in which the nonlinear unmodeled kinematics $\boldsymbol{\rho}_a$ is estimated online by a RBFNN and the external disturbance of the system $\boldsymbol{d}(k)$ is observed and suppressed through a DOB approach.

A. THE ONLINE LEARNING RBFNN

The RBFNN has been frequently used in mechanical systems to deal with model mismatch because of the universal approximation ability [31], [32]. The output of the RBFNN can be expressed as,

$$\hat{\boldsymbol{\rho}}_a(k) = \mathbf{W}^T\mathbf{H} \tag{29}$$

where $\mathbf{W} = [w_1, \ldots w_m]^T$ is the weight vector of the RBFNN, $\mathbf{H} = [h_1(\mathbf{y}), h_2(\mathbf{y}), \cdots, h_m(\mathbf{y})]^T$ is the activation function, and m is the hidden neurons number of RBFNN.

The Gaussian function is chosen as the activation function, which is given as below [33]

$$h_i(y) = \exp\left[-\frac{(y-c_i)^2}{2b_i^2}\right], \quad i = 1, 2, \cdots m \tag{30}$$

where c_i and b_i are the center and the width of the activation function respectively.

Assuming that there exists an ideal weight matrix $\mathbf{W}^* = [w_1, w_2, \cdots, w_m]^T$, the unmodeled kinematics $\boldsymbol{\rho}_a$ of the CPM can be expressed as,

$$\boldsymbol{\rho}_a = \mathbf{W}^{*T}\mathbf{H}(\mathbf{y}) + \varepsilon_d \tag{31}$$

where ε_d is the estimation error of the RBF neural network.

The adaptive law for the weights of the RBFNN is chosen as

$$\begin{aligned}\mathbf{W}_j(k+1) &= \mathbf{W}_j(k) + \Delta\mathbf{W}_j(k) \\ &= \mathbf{W}_j(k) + \eta e_j(k)\mathbf{H}^T(y)\end{aligned} \tag{32}$$

where η is a positive constant which represents the learning rate, and $\mathbf{e}(k)$ is the output error of the RBFNN which is given as

$$\mathbf{e}(k) = \boldsymbol{\rho}_a(k) - \hat{\boldsymbol{\rho}}_a(k) \tag{33}$$

Theorem: The value of $\hat{\boldsymbol{\rho}}_a(k)$ will converge to $\boldsymbol{\rho}_a(k)$ asymptotically if the learning rate η satisfies the following condition

$$0 < \eta < 2/\left\|\frac{\partial\hat{u}_j(k)}{\partial w_j(k)}\right\|^2 \tag{34}$$

Proof: Choose the following Lyapunov function:

$$V(k) = \frac{1}{2}\mathbf{e}(k)^2 = \frac{1}{2}\left(\boldsymbol{\rho}_a(k) - \hat{\boldsymbol{\rho}}_a(k)\right)^2 \tag{35}$$

Based on Eq(35) the increment of $V(k)$ can be obtained by,

$$\begin{aligned}\Delta V(k) &= V(k+1) - V(k) \\ &= \mathbf{e}(k)\Delta\mathbf{e}(k) + \frac{1}{2}\Delta\mathbf{e}(k)^2,\end{aligned} \tag{36}$$

where $\Delta\mathbf{e}(k)$ is the increment of the estimation error, which can be formulated as [34]

$$\Delta\mathbf{e}(k) = \left(\partial\mathbf{e}(k)/\partial\mathbf{W}(k)\right)^T\Delta\mathbf{W}(k) \tag{37}$$

According to Eq.(32), the following relationship can be found,

$$\begin{aligned}\Delta\mathbf{W}_j(k) &= \mathbf{W}_j(k+1) - \mathbf{W}_j(k) = -\eta\left(\frac{\partial E(k)}{\partial\mathbf{W}_j(k)}\right) \\ &= -\eta e_j(k)\frac{\partial e_j(k)}{\partial\mathbf{W}_j(k)} = \eta e_j(k)\frac{\partial\hat{\rho}_j(k)}{\partial\mathbf{W}_j(k)}\end{aligned} \tag{38}$$

Combining Eq.(37) and Eq.(38) with Eq.(36), $\Delta V(k)$ can be rewritten as,

$$\Delta V(k) = -\eta e_j^2(k) \times \left\|\frac{\partial\hat{\rho}_j(k)}{\partial\mathbf{W}_j(k)}\right\|^2 \times \left(1 - \frac{1}{2}\eta\left\|\frac{\partial\hat{\rho}_j(k)}{\partial\mathbf{W}_j(k)}\right\|^2\right) \tag{39}$$

It can be easily found that first term on the right part of Eq.(39) is negative, the second term is positive, and the last term is positive if the learning rate η satisfies the condition expressed in Eq.(34). The stability of the RBFNN is guaranteed, that is, the estimated $\hat{\boldsymbol{\rho}}_a(k)$ converges to the actual value of $\boldsymbol{\rho}_a(k)$ with any arbitrary accuracy.

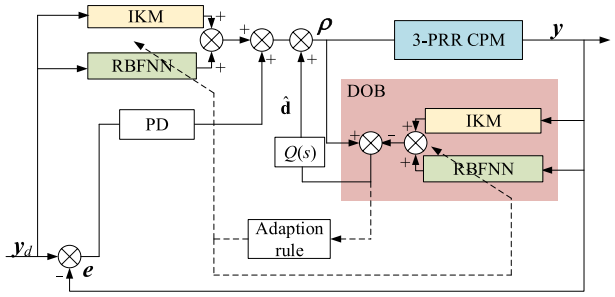

FIGURE 6. Block diagram of the control scheme.

B. CONTROL SCHEME DESIGN

The external disturbances $\mathbf{d}(k)$ can be calculated by rewriting Eq.(28) as,

$$\begin{aligned}\hat{\mathbf{d}}(k) &= \boldsymbol{\rho}(k) - \boldsymbol{\rho}_n(k) - \hat{\boldsymbol{\rho}}_a(k) \\ &= \boldsymbol{\rho}_a(k) + \mathbf{d}(k) - \hat{\boldsymbol{\rho}}_a(k)\end{aligned} \tag{40}$$

where $\hat{\mathbf{d}}(k)$ is the estimated disturbance. If the unmodeled factor of the system $\boldsymbol{\rho}_a(k)$ is accurately estimated by $\hat{\boldsymbol{\rho}}_a(k)$, i.e., the weight vector of RBFNN $\hat{\mathbf{W}}$ converges to $\mathbf{W}^*$, $\hat{\mathbf{d}}(k)$ can be expressed as below

$$\left|\lim_{\mathbf{W}\to\mathbf{W}^*}\hat{\mathbf{d}}(k) - \mathbf{d}(k)\right| = \left|\boldsymbol{\rho}_a(k) - \lim_{\mathbf{W}\to\mathbf{W}^*}\hat{\boldsymbol{\rho}}_a\right| < \varepsilon \tag{41}$$

Thus the observed disturbance $\hat{\mathbf{d}}$ will converge to its real value $\mathbf{d}$.

A block diagram of the proposed DOB-IKM control scheme is shown in Fig.6. An accurate inverse kinematic model is established by adding the output of the RBFNN $\hat{\boldsymbol{\rho}}_a(k)$ with the nominal inverse kinematic model $\boldsymbol{\rho}_n(k)$. The observed external disturbance $\hat{\mathbf{d}}(k)$ is compensated through a low pass filter $Q(s)$ to suppress the noise. Moreover, a typical PD controller is added in the feedback loop to improve the robustness of the controller.

V. EXPERIMENTAL TEST

A. THE EXPERIMENT SETUP

As shown in Fig.7, a prototype of the proposed CPM is fabricated using the optimized AEP notch shaped superelastic flexure hinge and the dimension parameters of the manipulator. The AEP superelastic flexure hinges are made of Nitinol. The fixed platform, the moving platform, and passive intermediate links of the CPM are made of Al-7075 alloy. The prismatic joint in the CPM is implemented by a linear stage which consists of a linear ultrasonic motor (LUSM, Nanomotion HR8), a linear guider, a linear grating encoder (Renishaw, RGH24O, 10nm resolution), and a slider. Unlike the frequently applied actuators in the compliant mechanisms, e.g., piezoelectric stack actuators or voice coil motors, the motion range of the LUSM is much larger, and most importantly, the LUSM consumes no energy while holding position (self-locking) [35], which is particularly suitable for CPM to maintain the motion accuracy during a long time period. The motion precision of the linear stage is

FIGURE 7. The experiment setup of the 3-PRR CPM (1. VTFP; 2. Moving target; 3. Laser displacement sensor-1; 4. Laser displacement sensor-2; 5. Laser displacement sensor-3; 6. Linear guide; 7. Slider; 8. LUSM; 9. Linear encoder; 10 LUSM based linear stage).

about 250nm under a sliding mode controller. In addition, the CPM is fixed on a vibration isolation table to decrease the influence of external disturbances.

A target block is fixed on the moving platform, and the output movement of the manipulator is captured by three laser displacement sensors (LDS), where LDS-1 (Keyence H050, measurement range: 20mm, resolution: 25nm) is arranged in the vertical direction of the target block, LDS-2 and LDS-3 (Keyence H020, measurement range: 6mm, resolution: 1nm) are arranged in the lateral direction of the target block.

As illustrated in Fig.8, the translation and rotation of the end-effector can be obtained as below,

$$\begin{cases}\varphi_p = \arctan\left(\dfrac{2\,L_3}{d_3 - d_2}\right) + \dfrac{\pi}{2} \\ \begin{pmatrix} x_p \\ y_p \end{pmatrix} = \begin{pmatrix} x_{A1} \\ y_{A1} \end{pmatrix} - R\left(\varphi_p\right)\begin{pmatrix} L_1/2 \\ L_2/2 \end{pmatrix},\end{cases} \tag{42}$$

where $d_1 d_2$ and d_3 are the displacements information acquired from the corresponding LDS, and L_1 and L_2 are the geometric parameters of the target block. The variables x_{A1} and y_{A1} are computed by

$$\begin{cases} x_{A1} = \dfrac{2L_3^2(L_1 - d_2 - d_3) + L_3(L_2 - 2d_1)(d_3 - d_2)}{4L_3^2 + (d_3 - d_2)^2} \\ y_{A1} = \dfrac{2L_3^2(L_2 - 2d_1) + L_3(d_3^2 - d_2^2 - d_3 L_1 + d_2 L_1)}{4L_3^2 + (d_3 - d_2)^2}, \end{cases} \tag{43}$$

where $2L_3$ is the distance between LDS-2 and LDS-3

A real-time control system is established by applying MATLAB xPC target toolbox and National Instruments (NI) data acquisition cards as illustrated in Fig.9. Command signals of the linear stages are generated through the DAC channels of a NI-6229 multifunction card, the displacement of the

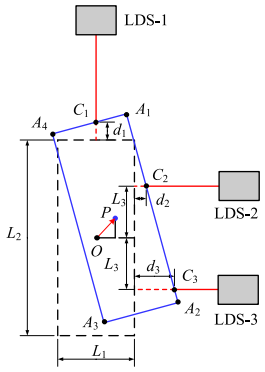

FIGURE 8. Schematic diagram of LDS arrangement.

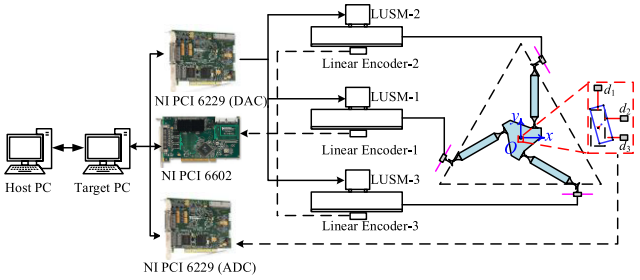

FIGURE 9. The hardware connection of the control system.

linear stages are obtained by a NI 6602 counter card, and the displacement information measured by LDSs are acquired through the ADC channels of the NI-6229 card. The tracking control algorithm is developed in MATLAB/Simulink on the host computer and then downloaded to the target computer.

The parameters for the online learning RBFNN are selected as follows: $m = 11$, $\mathbf{c}_j = 0.001 \times [-20, -16 \ldots, 0, \ldots, 16, 20]$ $(j = 1, 2, 3)$, $b_j = 0.01$, $\eta = 200$, the weight vector of the RBFNN is updated following Eq.(32). In addition, $Q(s)$ is selected as the first-order low-pass filter with a cut-off frequency of 20 Hz, the parameters of the PD controller are $\mathbf{K}_p = \text{diag}(100, 100, 60)$ and $\mathbf{K}_d = \text{diag}(20, 20, 10)$, and the sampling time of controller is 0.5 ms.

B. EXPERIMENTAL RESULTS

Experimental tests are carried out on the 3-PRR CPM prototype to investigate the motion resolution and the tracking performance of the CPM. For convenience, the horizontal and the vertical translations of the moving platform are denoted as D_x and D_y respectively and the rotation of the moving platform is denoted as R_z.

1) MOTION RESOLUTION

Consecutive step positioning is conducted on the proposed 3-PRR CPM to measure the resolution of the stage, and the results are presented in Fig.10-Fig.12. It can be seen that the translation resolution of the CPM is 0.2μm, and the rotation resolution is 0.002°. If the resolution of the LUSM and LDS can be further improved, a higher resolution of the proposed CPM could be achieved.

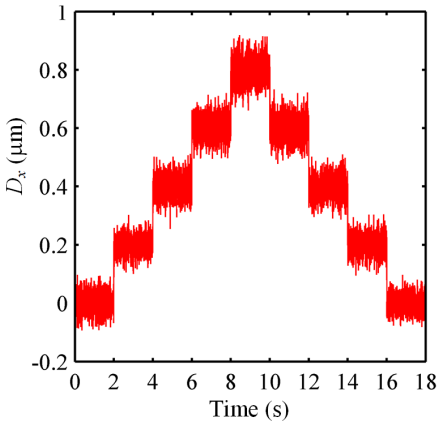

FIGURE 10. The translation path of the moving platform.

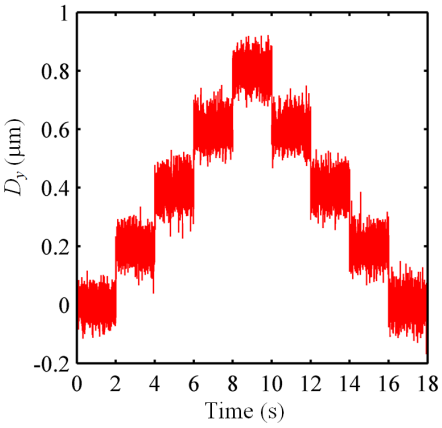

FIGURE 11. The rotation path of the moving platform.

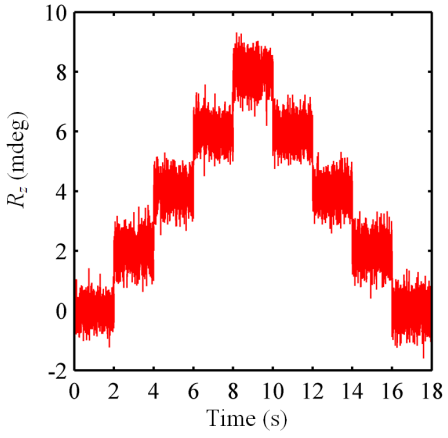

FIGURE 12. The tracking results of the DOB-IKM controller.

2) TRACKING PERFORMANCE

Since the available measurement range of the LDS cannot cover the entire regular workspace of the 3-PRR manipulator, a composite test trajectory which contains translation and rotation within the measurement range of the LDS is defined. The translation path of the moving platform is an ellipse,

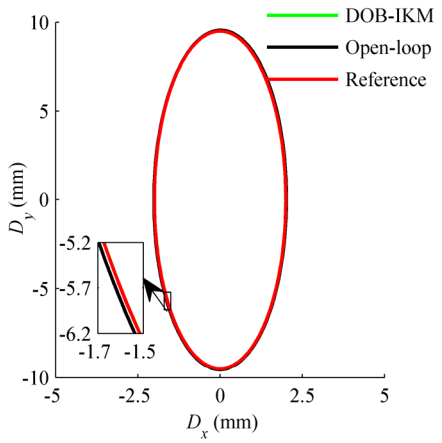

FIGURE 13. The translation path of the moving platform.

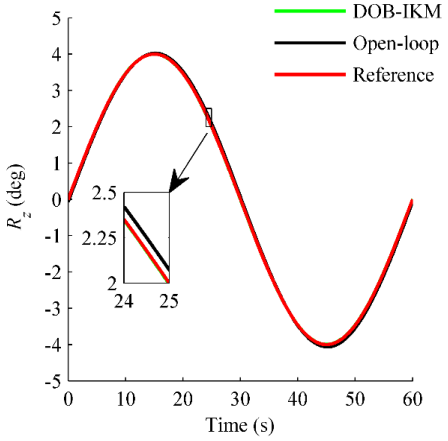

FIGURE 14. The rotation path of the moving platform.

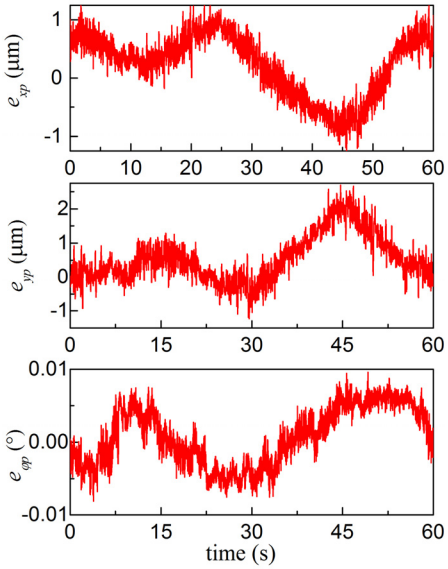

FIGURE 15. The tracking results of the DOB-IKM controller.

where the length for D_x is set as 9.5mm, the length for D_y is set as 2mm, and the path for R_z is set as a sinusoid with an amplitude of 4°, as presented in Fig.13 and Fig.14. The total time to complete the composite trajectory is 60 seconds. In addition, an open loop controller which uses the nominal inverse kinematic solution in section III is also implemented on the 3-PRR CPM.

TABLE 3. Tracking performance of different controllers.

Item	Error	EDOB-IKM	Open-loop controller
D_x	MAXE(μm)	1.312	22.786
	MAXE(%)	0.066	1.139
	RMSE(μm)	0.582	14.178
	RMSE(%)	0.029	0.709
D_y	MAXE(μm)	2.691	51.240
	MAXE(%)	0.028	0.539
	RMSE(μm)	0.880	35.551
	RMSE(%)	0.009	0.374
R_z	MAXE(°)	0.010	0.070
	MAXE(%)	0.250	1.750
	RMSE(°)	0.004	0.039
	RMSE(%)	0.100	0.975

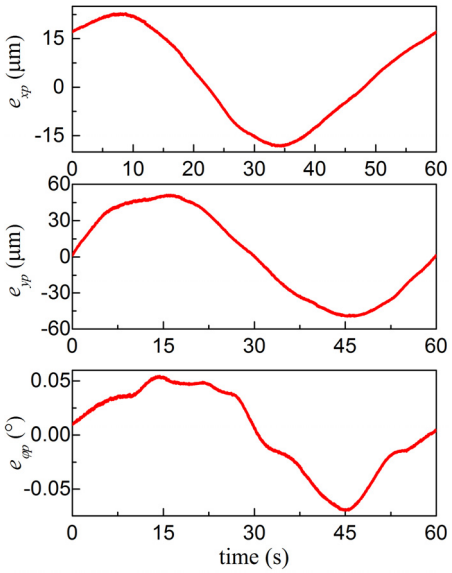

FIGURE 16. The tracking results of open-loop controller.

The experimental results are presented in Fig.13 through Fig.16, the maximum absolute error (MAXE) and the root mean square error (RMSE) of the deviation between the given trajectory and the actual trajectory of the manipulator are used to quantitatively analyze the performance of the controller. The MAXE and RMSE are defined as,

$$\text{MAXE} = \max\left(|e_i|\right); \quad \text{RMSE} = \sqrt{\frac{1}{N}\sum_{i=1}^{N} e_i^2}, \qquad (44)$$

where e_i is the corresponding tracking error, and N is the number of sampling points.

As summarized in Table 3, the DOB-IKM control scheme leads to a MAXE of 1.312μm, 2.691μm, and 0.010° for D_x, D_y and R_z respectively, which are equivalent to 0.066%,

0.029% and 0.250% of the motion range. The RMSE of the DOB-IKM control scheme is 0.582μm, 0.880μm and 0.004° for D_x, D_y and R_z respectively, which are 0.029%, 0.009% and 0.1% of the motion range. The performance of the open-loop controller on the other hand is significantly reduced, because of the unmodeled factors, such as the manufacturing uncertainties, the assembling error of the CPM, and external disturbances of the system. The MAXE of the open-loop control scheme is 22.786μm, 51.240μm, 0.070° for D_x, D_y and R_z respectively, i.e., 1.139%, 0.539% and 1.750 % of the motion range. The RMSE of the open-loop controller is 14.178μm, 35.551μm, 0.039° for D_x, D_y and R_z respectively, which is 0.709%, 0.374% and 0.975% of the motion range.

Therefore, the experimental test shows that the proposed control scheme is capable of compensating the model mismatch and suppressing external disturbance on the system.

VI. CONCLUSION

This paper presents a superelastic flexure hinge based planar 3-PRR CPM which is capable of achieving high precision with large regular workspace. A novel AEP notch shape which combines the advantages of ellipse profile and parabola profile is proposed, and the geometric parameters of the AEP superelastic flexure hinge are optimized by considering the rotation stiffness, the rotation error, and the variation of center shift simultaneously. A nominal inverse kinematic model of the CPM was established to provide a fast analytical kinematics solution for the optimization of the CPM. The dimension parameters of the 3-PRR manipulator were synthesized by maximizing the GCI of the manipulator over the regular workspace. A 3-PRR CPM prototype was fabricated based on the optimized AEP superelastic flexure hinges and dimensional parameters of the manipulator. The regular translation workspace of the designed CPM is a circle with radius of 10mm, and the rotation range of the CPM is ±5°, which is much larger than the conventional CPMs with notched flexure hinges.

A DOB-IKM control scheme which consists of an online learning adaptive RBFNN and a DOB is proposed to suppress the model mismatches and external disturbances of the 3-PRR CPM, where the RBFNN was designed to estimate the unmodeled kinematics of the 3-PRR CPM online, and the DOB approach was utilized to observe and compensate external disturbances of the system. Experimental results showed that the translation resolution of the CPM is 0.2μm, and the rotation resolution is 0.002°, furthermore, the proposed 3-PRR CPM could achieve micron scale translational tracking accuracy and micro-degree rotational tracking accuracy under the DOB-IKM control scheme.

REFERENCES

[1] Z. Du, R. Shi, and W. Dong, "A piezo-actuated high-precision flexible parallel pointing mechanism: Conceptual design, development, and experiments," *IEEE Trans. Robot.*, vol. 30, no. 1, pp. 131–137, Feb. 2014.

[2] K. Cai, T. Tian, X. Liu, S. Fatikow, F. Wang, L. Cui, D. Zhang, and B. Shirinzadeh, "Modeling and controller design of a 6-DOF precision positioning system," *Mech. Syst. Signal Process.*, vol. 104, pp. 536–555, May 2018.

[3] S. Shao, M. Xu, S. Zhang, and S. Xie, "Stroke maximizing and high efficient hysteresis hybrid modeling for a rhombic piezoelectric actuator," *Mech. Syst. Signal Process.*, vol. 75, pp. 631–647, Jun. 2016.

[4] J. Wen, N. Wan, R. Wang, S. Chen, J. Zheng, and J. Li, "A novel linear walking type piezoelectric actuator based on the parasitic motion of flexure mechanisms," *IEEE Access*, vol. 7, pp. 25908–25914, 2019.

[5] R. Cui, L. Chen, C. Yang, and M. Chen, "Extended state observer-based integral sliding mode control for an underwater robot with unknown disturbances and uncertain nonlinearities," *IEEE Trans. Ind. Electron.*, vol. 64, no. 8, pp. 6785–6795, Aug. 2017.

[6] M. Naves, D. M. Brouwer, and R. G. K. M. Aarts, "Building block-based spatial topology synthesis method for large-stroke flexure hinges," *J. Mech. Robot.*, vol. 9, no. 4, 2017, Art. no. 041006.

[7] H. Yu, C. Zhang, B. Yang, S. Chen, and G. Yang, "Design and analysis of a large-range flexure-based parallel mechanism based on matrix method," in *Proc. IEEE/ASME Int. Conf. Adv. Intell. Mechatronics (AIM)*, Jul. 2018, pp. 762–767.

[8] A. Raatz, F. Trauden, and J. Hesselbach, "Modeling compliant parallel robots," in *Proc. ASME Int. Design Eng. Tech. Conf. Comput. Inf. Eng. Conf.*, 2006, pp. 65–76.

[9] M. Wu, F. Yang, Y. Lu, J. Wang, G. Wang, H. Yue, and H. Yu, "Compliance analysis for flow effector actuator based on serial compliant mechanism with double guide ends," *IEEE Access*, vol. 7, pp. 28913–28928, 2019.

[10] M. Yang, Z. Du, and W. Dong, "Modeling and analysis of planar symmetric superelastic flexure hinges," *Precis. Eng.*, vol. 46, pp. 177–183, Oct. 2015.

[11] Z. Du, M. Yang, W. Dong, and D. Zhang, "Static deformation modeling and analysis of flexure hinges made of a shape memory alloy," *Smart Mater. Struct.*, vol. 25, no. 11, 2016, Art. no. 115029.

[12] Y. K. Yong, T.-F. Lu, and D. C. Handley, "Review of circular flexure hinge design equations and derivation of empirical formulations," *Precis. Eng.*, vol. 32, no. 2, pp. 63–70, Apr. 2008.

[13] G. Chen, X. Shao, and X. Huang, "A new generalized model for elliptical arc flexure hinges," *Rev. Sci. Instrum.*, vol. 79, no. 9, 2008, Art. no. 095103.

[14] N. Lobontiu, J. S. N. Paine, E. Garcia, and M. Goldfarb, "Design of symmetric conic-section flexure hinges based on closed-form compliance equations," *Mech. Mach. Theory*, vol. 37, no. 5, pp. 477–498, May 2002.

[15] S. Zelenika, M. G. Munteanu, and F. De Bona, "Optimized flexural hinge shapes for microsystems and high-precision applications," *Mech. Mach. Theory*, vol. 44, no. 10, pp. 1826–1839, 2009.

[16] J. L. Chen, C. L. Zhang, M. L. Xu, Y. Y. Zi, and X. N. Zhang, "Rhombic micro-displacement amplifier for piezoelectric actuator and its linear and hybrid model," *Mech. Syst. Signal Process.*, vols. 50–51, pp. 580–593, Jan. 2015.

[17] M. T. Masouleh and C. M. Gosselin, "Determination of singularity-free zones in the workspace of planar 3-P_RR parallel ," *J. Mech. Des.*, vol. 129, no. 6, pp. 649–652, 2007.

[18] Z. Zhan, X. Zhang, Z. Jian, and H. Zhang, "Error modelling and motion reliability analysis of a planar parallel manipulator with multiple uncertainties," *Mech. Mach. Theory*, vol. 124, pp. 55–72, Jun. 2018.

[19] Y. Su, W. Dong, Y. Wu, Z. Du, and Y. Demiris, "Increasing the accuracy and the repeatability of position control for micromanipulations using Heteroscedastic Gaussian Processes," in *Proc. IEEE Int. Conf. Robot. Autom.*, May/Jun. 2014, pp. 4692–4698.

[20] Q. Xu, "Design, testing and precision control of a novel long-stroke flexure micropositioning system," *Mechanism Mach. Theory*, vol. 70, pp. 209–224, Dec. 2013.

[21] Y. Singh, V. Vinoth, Y. R. Kiran, J. K. Mohanta, and S. Mohan, "Inverse dynamics and control of a 3-DOF planar parallel (U-shaped 3-PPR) manipulator," *Robot. Comput.-Integr. Manuf.*, vol. 34, pp. 164–179, Aug. 2015.

[22] G. Wang and Q. Xu, "Adaptive terminal sliding mode control for motion tracking of a micropositioning system," *Asian J. Control*, vol. 20, no. 3, pp. 1241–1252, 2017.

[23] Z. Ding, F. Zhao, Y. Lang, Z. Jiang, and J. Zhu, "Anti-disturbance neural-sliding mode control for inertially stabilized platform with actuator saturation," *IEEE Access*, vol. 7, pp. 92220–92231, 2019.

[24] J. Ye, J. Yang, D. Xie, B. Huang, and H. Cai, "Strong robust and optimal chaos control for permanent magnet linear synchronous motor," *IEEE Access*, vol. 7, pp. 57907–57916, 2019.

[25] R. Wang, X. Zhou, and Z. Zhu, "Development of a novel sort of exponent-sine-shaped flexure hinges," *Rev. Sci. Instrum.*, vol. 84, no. 9, 2013, Art. no. 095008.

[26] M. Yang, Z. Du, W. Dong, and L. Sun, "Design and modeling of a variable thickness flexure pivot," *J. Mech. Robot.*, vol. 11, no. 1, Oct. 2018, Art. no. 014502.
[27] M. Yang, Z. Du, F. Chen, W. Dong, and D. Zhang, "Kinetostatic modelling of a 3-PRR planar compliant parallel manipulator with flexure pivots," *Precis. Eng.*, vol. 48, pp. 323–330, Apr. 2017.
[28] J. Zhao, T. Yang, Z. Ma, C. Yang, Z. Wang, and C. Wang, "Energy consumption minimizing for electro-hydraulic servo driving planar parallel mechanism by optimizing the structure based on genetic algorithm," *IEEE Access*, vol. 7, pp. 47090–47101, 2019.
[29] L. Xu, Q. Chen, L. He, and Q. Li, "Kinematic analysis and design of a novel 3T1R 2-$(PRR)^2$RH hybrid manipulator," *Mech. Mach. Theory*, vol. 112, pp. 105–122, Jun. 2017.
[30] R. S. Stoughton and T. Arai, "A modified Stewart platform manipulator with improved dexterity," *IEEE Trans. Robot. Autom.*, vol. 9, no. 2, pp. 166–173, Apr. 1993.
[31] Q. Chen, X. Ren, J. Na, and D. Zheng, "Adaptive robust finite-time neural control of uncertain PMSM servo system with nonlinear dead zone," *Neural Comput. Appl.*, vol. 28, no. 12, pp. 3725–3736, 2016.
[32] M. D. Tran and H. J. Kang, "A novel adaptive finite-time tracking control for robotic manipulators using nonsingular terminal sliding mode and RBF neural networks," *Int. J. Precis. Eng. Manuf.*, vol. 17, no. 7, pp. 863–870, Jul. 2016.
[33] W. Yan, S. Hou, Y. Fang, and J. Fei, "Robust adaptive nonsingular terminal sliding mode control of MEMS gyroscope using fuzzy-neural-network compensator," *Int. J. Mach. Learn. Cybern.*, vol. 8, no. 4, pp. 1287–1299, 2017.
[34] B. Vatankhah and M. Farrokhi, "Nonlinear model-predictive control with disturbance rejection property using adaptive neural networks," *J. Franklin Inst.*, vol. 354, no. 13, pp. 5201–5220, 2017.
[35] F.-J. Lin, S.-Y. Chen, K.-K. Shyu, and Y.-H. Liu, "Intelligent complementary sliding-mode control for LUSMs-based X-Y-θ motion control stage," *IEEE Trans. Ultrason., Ferroelectr., Freq. Control*, vol. 57, no. 7, pp. 1626–1640, Jul. 2010.

MIAO YANG received the B.E. degree in mechanical engineering from the Wuhan University of Science and Technology, Wuhan, China, in 2012, and the M.E. and Ph.D. degrees from the Harbin Institute of Technology (HIT), Harbin, China, in 2014 and 2019, respectively. He is currently a Postdoctoral Researcher at the Ningbo Institute of Materials Technology and Engineering, CAS. His current research interests include long stroke compliant mechanism, precision motion control, and robotics for precision manipulation.

CHI ZHANG received the B.E. and M.E. degrees from Xi'an Jiaotong University, in 1999 and 2002, respectively, and the Ph.D. degree from Nanyang Technological University, Singapore, in 2007, all in electrical and electronic engineering. He is currently a Professor with the Ningbo Institute of Materials Technology and Engineering, CAS. His current research interests include precise actuator design, precision motion control, permanent magnet motor and its control, advanced robotics, and intelligent manufacturing equipment.

GUILIN YANG received the B.E. and M.E. degrees from the Jilin University of Technology, Jilin, China, in 1985 and 1988, respectively, and the Ph.D. degree from Nanyang Technological University, Singapore, in 1999. He is currently the Director of the Zhejiang Key Laboratory of Robotics and Intelligent Manufacturing Equipment Technology, Ningbo Institute of Materials Technology and Engineering, CAS, and a Professor of the University of Chinese Academy of Sciences, Beijing, China. He has published more than 270 research articles which have been cited more than 3000 times. His research interests include mechanism and machine design, modular robotic systems, and robot navigation.

WEI DONG received the B.E. and Ph.D. degrees in mechanical engineering from the Harbin Institute of Technology (HIT), Harbin, China, in 2001 and 2007, respectively. He worked as a Postdoctoral Researcher at CNRS FEMTO-ST, France, from 2009 to 2010, and the Department of Mechanical Engineering, University of Connecticut, Storrs, CT, USA, from 2007 to 2009, respectively. He is currently a Full Professor with the State Key Laboratory of Robotics and System, HIT. His current research interests include innovative design of robot/mechatronics systems, robotic system modeling and optimization, and smart material and structure integration and applications.